High-performance chiral mirrors by twisted anisotropic photonic crystals

Andrea Alessandrini,[1] Leone di Mauro Villari,[1] Luca Assogna,[1] Matteo Silvestri,[1] Matteo Venturi,[1] Carino Ferrante,[2] Paola Benassi,[1,2] Davide Tedeschi,[1] and Andrea Marini[1,2,*]

[1] *Department of Physical and Chemical Sciences, University of L'Aquila, Via Vetoio, L'Aquila 67100, Italy*

[2] *CNR-SPIN, c/o Department of Physical and Chemical Sciences, Via Vetoio, Coppito (L'Aquila) 67100, Italy*

(Received 4 February 2025; revised 15 April 2025; accepted 6 May 2025; published 11 June 2025)

The capability of anisotropic media to exert an optical torque on electromagnetic fields is crucial for polarization control. Here we investigate twisted layered stacks of uniaxial anisotropic media to engineer chiral mirrors for the manipulation of circularly polarized light by adjusting the layer number, thicknesses, and orientation. To this aim, we undertake a comprehensive theoretical analysis devising a multilayered twisted anisotropic photonic crystal enabling highly efficient circular polarization manipulation functionalities, i.e., showing concurring close-to-unitary helicity-preserving reflectance of one circular polarization and transmittance of the opposite one. Owing to the angular-momentum manipulation concept enabled by our proposed devices, we envisage that such chiral mirrors are promising candidates for an alternative class of integrated circular polarizers, holding great potential for applications in quantum technologies, polarization-sensitive optical detectors, and electro-optical information processing.

DOI: 10.1103/PhysRevApplied.23.064027

I. INTRODUCTION

A system is said to be chiral if it can not be superposed onto its mirror image by any translation or rotation. Chiroptical effects, such as circular dichroism (CD) [1–3] and optical rotation dispersion (ORD) [3], are produced via the interaction between circularly polarized (CP) light and chiral matter. However, chiral molecules show a weak chiroptical response owing to their subwavelength size preventing efficient magnetic-dipole interactions [4]. Consequently, metamaterials (MMs) and metasurfaces (MSs) have received a growing interest in the field of chiral photonics due to their significantly enhanced chiroptical responses if compared with natural materials [5–7], allowing for the realization of ultracompact devices for CP light generation, manipulation, and detection.

The helicity of light plays a crucial role in both classical and quantum optics. In particular, chiroptical spectroscopies heavily rely on CP control to discriminate enantiomeric excess of solvated chiral molecules. It is well known that a standard achiral mirror flips light helicity upon reflection owing to total angular-momentum (AM) conservation. This holds true for both simple electric mirrors and MM-based magnetic mirrors [8–10], which reverse the direction of the reflected electric and magnetic fields, respectively. Helicity-preserving mirrors have been designed to improve control and manipulation of light polarization [11–13]. Chiral MMs, e.g., based on gold helices fabricated by direct laser writing [14], have been further employed in the realization of circular polarizers [15] that can block CP waves with a given handedness while transmitting the other [14]. Fabrication methods, other than direct laser writing, include *e*-beam lithography and focused-ion beam milling, enabling the fabrication of nanophotonic structures preserving materials compatibility, scalability, and integration with existing devices [7,16,17].

Recently, two-dimensional (2D) chiral plasmonic and dielectric MSs [7] and stacks of twisted structures [15,18–21] with chiro-optical properties have been reported. Plasmonic chiral MSs are based on metals and exhibit strong light-matter interaction due to surface-plasmon resonances [7,22,23], which increase the efficiency of sensing and optical frequency-conversion applications. Moreover, metallic mirrors reflect light over a broad range of frequencies incident from arbitrary angles. However, high absorption and Ohmic losses limit their performance [7] and a few percent of the incident power gets lost at infrared and optical frequencies [24]. Conversely, dielectric chiral MSs exhibit weak absorption losses [7,25] and their functionality stems from Mie resonances of high-refractive index dielectric nanostructures [26,27]. They have several applications spanning from the control of CP

*Contact author: andrea.marini@univaq.it

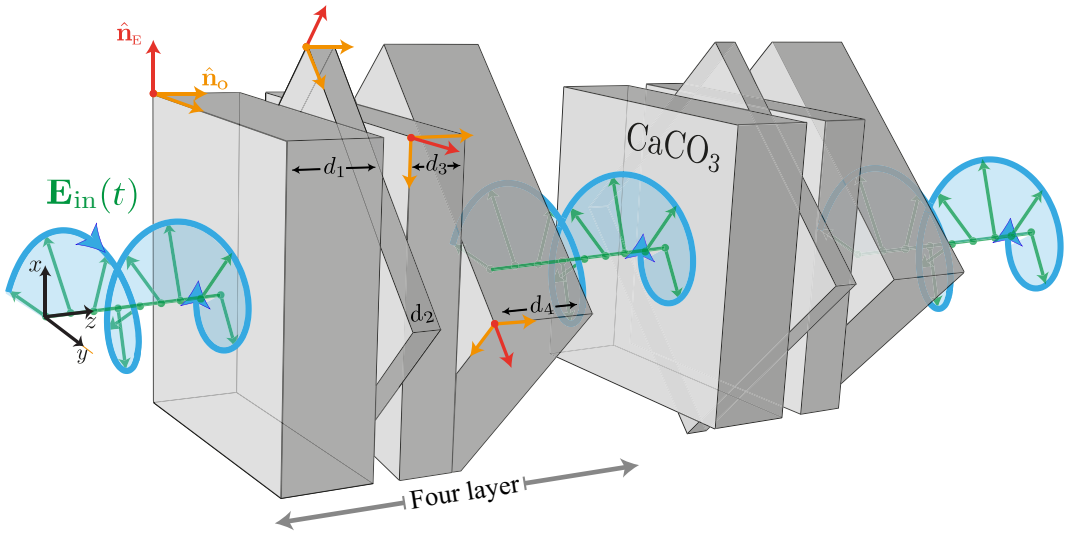

FIG. 1. Schematic of the optical system with $N \times 4$-layer stacks of uniaxial anisotropic media of $CaCO_3$. Each layer in every stack has a specific thickness and a certain extraordinary angle θ_E with respect to the x axis, which progressively rotates right handedly by $\Delta\theta_E = \pi/4$. The mirror is illuminated by an EM field $\mathbf{E}_{in}(t)$ with arbitrary vacuum wavelength, incidence angle, and impinging polarization. For the sake of simplicity, the illustration shows a normally incident right CP EM field.

light [28], vortex generation, and manipulation [29,30] to spin-selective reflectors [31–33].

In this paper, we introduce another concept for radiation AM manipulation by devising twisted anisotropic photonic crystals (TAPCs) for CP manipulation functionalities. In particular, we engineer a chiral mirror working concurrently as a CP diode for one polarization, i.e., transmitting efficiently CP light with a specific helicity, and as a helicity-preserving mirror for the opposite one. To this end, we properly adjust the TAPC layer number, thicknesses, and orientation of extraordinary axes, as schematically depicted in Fig. 1. CP optical diode functionalities have already been reported by cholesteric liquid crystals [34] and MMs based on dielectric helices [35], circumventing problems of plasmonic nanostructures. However, we emphasize that the devised TAPCs reported here do not solely transmit one CP while blocking the opposite CP, which is actually reflected with close-to-unitary (CTU) efficiency while conserving its helicity, conversely to standard achiral mirrors. Moreover, owing to the flat interfaces of our proposed TAPCs, one can engineer the CP-selective reflectance and transmittance bandwidths from the near UV to the near IR by properly adjusting the layer thicknesses. The TAPC AM manipulation is attained by engineering of the torque volume density $\boldsymbol{\tau}_V^{pol} = \mathbf{P} \times \mathbf{E} = \mathbf{D} \times \mathbf{E}$ [36], where $\mathbf{D} = \varepsilon_0 \mathbf{E} + \mathbf{P}$ is the displacement vector embedding the electric field $\mathbf{E}$ acting self-consistently on the polarization $\mathbf{P}$ of the medium. Due to conservation of the total AM of the full system [electromagnetic (EM) field plus the chiral mirror], the field itself is subject to the opposite optical torque density $\boldsymbol{\tau}_V^{EM} = -\mathbf{D} \times \mathbf{E}$. This mechanism favors the transmission of one CP component with respect to the other within each anisotropic layer with a fixed thickness. To devise the TAPC functionalities, we perform a comprehensive theoretical analysis by considering an impinging monochromatic plane EM wave with arbitrary incidence angle, polarization, and wavelength. Our theoretical model is based on the well-established EM transfer-matrix approach to birefringent layered media [37–39]. By specializing our model to anisotropic layers of calcite ($CaCO_3$), we numerically assess the optimal layer properties to concurrently maximize transmittance of a specific impinging helicity and reflectance of the opposite one. Remarkably, we find realistic physical parameters enabling >99% CP-sensitive reflectance, indicating that TAPCs constitute a promising candidate for polarization control at the microscale, enabling future CP-sensitive splitters, diodes, and cavities.

The paper is organized as follows. In Sec. II we investigate the mechanical effects produced by a single anisotropic layer of calcite ($CaCO_3$), i.e., a standard quarter-wave plate, on the impinging EM field polarization, illustrating the pathways towards its manipulation. In Sec. III we design a TAPC composed of a series of $N \times 4$ layers of progressively rotated $CaCO_3$ crystals, see Fig. 1, where thicknesses can be optimized to impart the appropriate phase to each EM field component within each layer, enabling our device to concurrently act as a highly efficient CP diode for one CP and as a helicity-preserving mirror for the opposite one.

II. SINGLE ANISOTROPIC LAYER

We first consider a monochromatic EM field with angular frequency ω, impinging from vacuum on an uniaxial anisotropic medium, i.e., a quarter-wave plate. In our calculations we focus on $CaCO_3$ [40] thanks to its optimal refractive-index step, characterized by the ratio $|\Delta n(\omega)|/\bar{n}(\omega)$, where $\Delta n(\omega) = n_{\rm E}(\omega) - n_{\rm O}(\omega)$, $\bar{n}(\omega) = [n_{\rm E}(\omega) + n_{\rm O}(\omega)]/2$, and $n_{\rm E,O}$ indicate the extraordinary (E) and ordinary (O) refractive indices, see Fig. 2(a). We first solve Maxwell's equations in vacuum for an arbitrary direction of propagation, expressing the solution in the basis of left and right CP light (LCP and RCP light, respectively). Thus, for $z < 0$, the EM field is given by

$$\mathbf{E}_{\rm vac}(\mathbf{r},t) = \sum_{s=\pm1} \mathrm{Re}\left\{\left[A_s^{(\rm I)}\hat{\mathbf{n}}_s^{(\rm I)} e^{i\mathbf{k}_{\rm I}\cdot\mathbf{r}} + A_s^{(\rm R)}\hat{\mathbf{n}}_s^{(\rm R)} e^{i\mathbf{k}_{\rm R}\cdot\mathbf{r}}\right] e^{-i\omega t}\right\},$$

$$\mathbf{H}_{\rm vac}(\mathbf{r},t) = \sum_{s=\pm1} \mathrm{Re}\left\{\frac{s}{i\mu_0 c}\left[A_s^{(\rm I)}\hat{\mathbf{n}}_s^{(\rm I)} e^{i\mathbf{k}_{\rm I}\cdot\mathbf{r}} + A_s^{(\rm R)}\hat{\mathbf{n}}_s^{(\rm R)} e^{i\mathbf{k}_{\rm R}\cdot\mathbf{r}}\right] e^{-i\omega t}\right\}, \quad (1)$$

where c is the speed of light in vacuum, μ_0 is the vacuum permittivity, $\mathbf{k}_{\rm I} = k_{\rm Ix}\hat{\mathbf{e}}_x + k_{\rm Iy}\hat{\mathbf{e}}_y + k_{\rm Iz}\hat{\mathbf{e}}_z$ and $\mathbf{k}_{\rm R} = k_{\rm Ix}\hat{\mathbf{e}}_x + k_{\rm Iy}\hat{\mathbf{e}}_y - k_{\rm Iz}\hat{\mathbf{e}}_z$ are the incident and reflected wave vectors, respectively, the indices I(R) indicate incident (reflected) waves, $s = \pm1$ refer to the right ($s = 1$) and left ($s = -1$) CP waves, $\hat{\mathbf{n}}_s^{(\rm I,R)}$ are CP unit vectors of impinging and reflected waves with CP index s, and $\hat{\mathbf{e}}_{x,y,z}$ are the x, y, z axes unit vectors. Note that the reflected wave vector satisfies the conservation of the transversal component $\mathbf{k}_{\rm I\perp} = k_{\rm Ix}\hat{\mathbf{e}}_x + k_{\rm Iy}\hat{\mathbf{e}}_y$ arising from translational invariance of the system in the x-y plane. Moreover, Maxwell's equations for impinging and reflected waves imply the dispersion relation $|\mathbf{k}_{\rm I}|^2 = |\mathbf{k}_{\rm R}|^2 = \omega^2/c^2$.

Then, we solve Maxwell's equations inside a single $CaCO_3$ layer with orientation illustrated in Fig. 2(a) and thickness d, obtaining

$$\mathbf{E}_{\rm an}^{(\pm)}(\mathbf{r},t) = \sum_{\xi}\sum_{l=1}^{2} \mathrm{Re}\left[E_\xi^{(l,\pm)}(z)\hat{\mathbf{e}}_\xi e^{i\mathbf{k}_{\rm I\perp}\cdot\mathbf{r} - i\omega t}\right], \quad (2a)$$

$$\mathbf{H}_{\rm an}^{(\pm)}(\mathbf{r},t) = \sum_{\xi}\sum_{l=1}^{2} \mathrm{Re}\left[H_\xi^{(l,\pm)}(z)\hat{\mathbf{e}}_\xi e^{i\mathbf{k}_{\rm I\perp}\cdot\mathbf{r} - i\omega t}\right], \quad (2b)$$

where $\xi = x, y, z$, the index $l = 1, 2$ refers to one of the two propagation modes within the anisotropic medium,

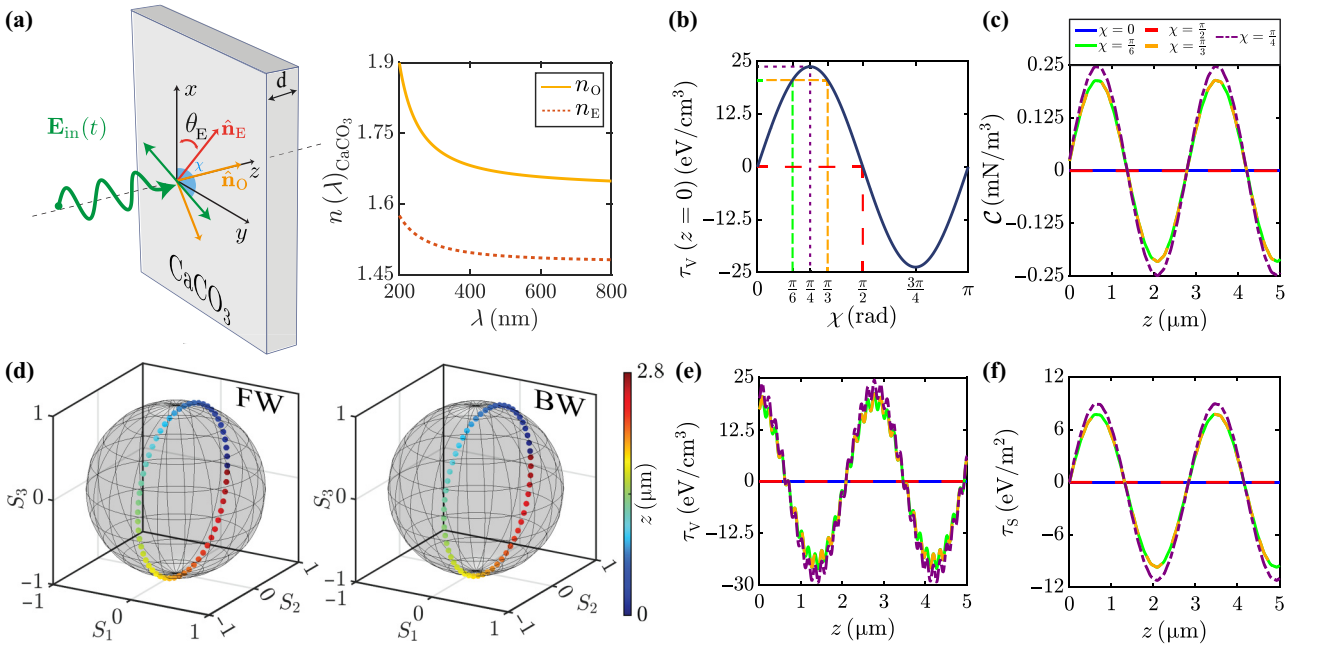

FIG. 2. EM field propagation within a uniaxial anisotropic medium. (a) On the left, schematic of a uniaxial anisotropic slab of $CaCO_3$ with thickness $d = 5$ μm and a fixed extraordinary angle $\theta_{\rm E} = 0$ with respect to the x axis, normally illuminated by an EM field $\mathbf{E}_{\rm in}(t)$ with vacuum wavelength $\lambda = 500$ nm and linear polarization forming a χ angle with the x direction. The inset on the right illustrates the wavelength dependence of the ordinary ($n_{\rm O}$) and extraordinary ($n_{\rm E}$) refractive indexes of $CaCO_3$ [40]. (b) Dependence of the optical torque density over the LP angle χ, exerted by the medium on the EM field, upon refraction by the medium in $z = 0$. (c) Dependence of the optical chirality $\mathcal{C}$ over the propagation coordinate z for distinct impinging LP angles χ. (d) Dependence of the forward and backward (FW and BW) EM fields' Stokes parameters on z for $\chi = \pi/4$. (e),(f) Dependence of (e) the optical torque volume density and (f) the effective optical torque per unit surface on z for several distinct impinging LP angles χ, see the upper-right color legend.

and $\pm$ indicates forward and backward propagating waves, respectively. From Maxwell's equations we retrieve the following system of coupled ordinary differential equations for the EM field components:

$$\frac{d^2E_p^{(l,\pm)}}{dz^2} - ik_{\mathrm{I}p}\frac{dE_z^{(l,\pm)}}{dz} = \left[k_{\mathrm{I}q}^2 - \frac{\omega^2}{c^2}\varepsilon_{pp}\right]E_x^{(l,\pm)} - \left[\frac{\omega^2}{c^2}\varepsilon_{pq} + k_{\mathrm{I}p}k_{\mathrm{I}q}\right]E_q^{(l,\pm)}, \tag{3a}$$

$$k_{\mathrm{I}x}\frac{dE_x^{(l,\pm)}}{dz} + k_{\mathrm{I}y}\frac{dE_y^{(l,\pm)}}{dz} = i\left[|\mathbf{k}_{\mathrm{I}\perp}|^2 - \frac{\omega^2}{c^2}\varepsilon_{zz}\right]E_z^{(l,\pm)}, \tag{3b}$$

where $p,q = x,y$, $\varepsilon_{xx} = \varepsilon_{\mathrm{E}}\cos^2\theta_{\mathrm{E}} + \varepsilon_{\mathrm{O}}\sin^2\theta_{\mathrm{E}}$, $\varepsilon_{xy} = \varepsilon_{yx} = (\varepsilon_{\mathrm{E}} - \varepsilon_{\mathrm{O}})\sin\theta_{\mathrm{E}}\cos\theta_{\mathrm{E}}$, $\varepsilon_{yy} = \varepsilon_{\mathrm{E}}\sin^2\theta_{\mathrm{E}} + \varepsilon_{\mathrm{O}}\cos^2\theta_{\mathrm{E}}$, $\varepsilon_{zz} = \varepsilon_{\mathrm{O}}$, and θ_{E} is the extraordinary angle, i.e., the angle between the extraordinary and the x axes, see Fig. 2(a). In such expressions $\varepsilon_{\mathrm{O,E}} = n_{\mathrm{O,E}}^2$ are the ordinary and extraordinary relative dielectric constants along the directions that diagonalize the dielectric tensor of the anisotropic medium. With the ansatz $E_{x,y,z}^{(l,\pm)} = C_{x,y,z}^{(l,\pm)}e^{\pm i\beta_l z}$, we find the normalized eigenmodes

$$\begin{aligned} C_x^{(1,\pm)} &= \sin\theta_{\mathrm{E}}\beta_1 A_1^{(\pm)}/D_1, \\ C_y^{(1,\pm)} &= -\cos\theta_{\mathrm{E}}\beta_1 A_1^{(\pm)}/D_1, \\ C_z^{(1,\pm)} &= \pm\gamma(\mathbf{k}_{\mathrm{I}\perp},\theta_{\mathrm{E}})A_1^{(\pm)}/D_1, \end{aligned} \tag{4}$$

where $D_1 = \left[(\omega^2/c^2)\varepsilon_{\mathrm{O}} - \alpha^2(\mathbf{k}_{\mathrm{I}\perp},\theta_{\mathrm{E}})\right]^{1/2}$, and $\beta_1 = \left[(\omega^2/c^2)\varepsilon_{\mathrm{O}} - |\mathbf{k}_{\mathrm{I}\perp}|^2\right]^{1/2}$. Similarly, for the $C_{x,y,z}^{(2,\pm)}$ mode we find

$$\begin{aligned} C_x^{(2,\pm)} &= \left[\frac{\omega^2}{c^2}\cos\theta_{\mathrm{E}} - \frac{k_{\mathrm{I}x}}{\varepsilon_{\mathrm{O}}}\alpha(\mathbf{k}_{\mathrm{I}\perp},\theta_{\mathrm{E}})\right]A_2^{(\pm)}/D_2, \\ C_y^{(2,\pm)} &= \left[\frac{\omega^2}{c^2}\sin\theta_{\mathrm{E}} - \frac{k_{\mathrm{I}y}}{\varepsilon_{\mathrm{O}}}\alpha(\mathbf{k}_{\mathrm{I}\perp},\theta_{\mathrm{E}})\right]A_2^{(\pm)}/D_2, \\ C_z^{(2,\pm)} &= \mp\frac{1}{\varepsilon_{\mathrm{O}}}\alpha(\mathbf{k}_{\mathrm{I}\perp},\theta_{\mathrm{E}})\,\beta_2 A_2^{(\pm)}/D_2, \end{aligned} \tag{5}$$

where

$$D_2 = \left[(\omega^2/c^2) - \varepsilon_{\mathrm{O}}^{-1}\alpha^2(\mathbf{k}_{\mathrm{I}\perp},\theta_{\mathrm{E}})\right]^{1/2} \times \left[(\omega^2/c^2) + (\varepsilon_{\mathrm{E}} - \varepsilon_{\mathrm{O}})\alpha^2(\mathbf{k}_{\mathrm{I}\perp},\theta_{\mathrm{E}})/\varepsilon_{\mathrm{O}}^2\right]^{1/2}, \tag{6}$$

and $\beta_2 = [(\omega^2/c^2)\varepsilon_{\mathrm{E}} - (\varepsilon_{\mathrm{E}}/\varepsilon_{\mathrm{O}})\alpha^2(\mathbf{k}_{\mathrm{I}\perp},\theta_{\mathrm{E}}) - \gamma^2(\mathbf{k}_{\mathrm{I}\perp},\theta_{\mathrm{E}})]^{1/2}$. In such expressions we have defined the functions $\alpha(\mathbf{k}_{\mathrm{I}\perp},\theta_{\mathrm{E}}) = k_{\mathrm{I}x}\cos\theta_{\mathrm{E}} + k_{\mathrm{I}y}\sin\theta_{\mathrm{E}}$ and $\gamma(\mathbf{k}_{\mathrm{I}\perp},\theta_{\mathrm{E}}) = -k_{\mathrm{I}x}\sin\theta_{\mathrm{E}} + k_{\mathrm{I}y}\cos\theta_{\mathrm{E}}$. We are now able to investigate the effects of anisotropy on the polarization of reflected and refracted EM fields. We begin our analysis with linearly polarized (LP) waves (with LP angle χ with respect to the x axis) impinging at normal incidence on a single layer of $CaCO_3$, see Fig. 2(a). Owing to linearity, for the sake of simplicity we assume an impinging electric-field amplitude $|\mathbf{E}_{\mathrm{in}}| = \sqrt{2}$ V/m. Figure 2(b) shows the dependence of the optical torque density on the LP angle at $z = 0$. Note that, for χ ranging from 0 to $\pi/2$, the EM field is subject to a positive torque density. Conversely, for χ ranging from $\pi/2$ to π, the torque becomes negative. This implies that the anisotropic medium is forcing the field to acquire RCP for $0 < \chi < \pi/2$ and LCP for $\pi/2 < \chi < \pi$. Moreover, the maximum absolute value of the torque density is associated to $\chi = \pi/4, 3\pi/4$, while for $\chi = 0, \pi/2$ the torque density vanishes since the fields are polarized along the in plane principal axis for $\theta_{\mathrm{E}} = 0$, and thus are eigenstates of the vectorial problem. This result can be better understood in terms of time averages of the torque density at $z = 0$

$$\langle\boldsymbol{\tau}_{\mathrm{V}}^{\mathrm{EM}}\rangle_T = \frac{\varepsilon_0|\mathbf{E}_{\mathrm{in}}|^2}{8G_{\mathrm{O}}^{(+)}G_{\mathrm{E}}^{(+)}}\left[\left(G_{\mathrm{O}}^{(+)}\right)^2 - \left(G_{\mathrm{O}}^{(-)}\right)^2\right]\left[\left(G_{\mathrm{E}}^{(+)}\right)^2 + - \left(G_{\mathrm{E}}^{(-)}\right)^2\right](\varepsilon_{\mathrm{E}} - \varepsilon_{\mathrm{O}})\sin\left[2\,(\theta_{\mathrm{E}} - \chi)\right]\hat{\mathbf{e}}_z, \tag{7}$$

where $G_{\mathrm{O}}^{(\pm)} = 1 \pm 1/\sqrt{\varepsilon_{\mathrm{O}}}$ and $G_{\mathrm{E}}^{(\pm)} = 1 \pm 1/\sqrt{\varepsilon_{\mathrm{E}}}$. This expression clearly indicates that the sign of the torque density depends on the angle between the extraordinary axis and the polarization direction, and on the difference between ε_{E} and ε_{O}, which for $CaCO_3$ at $\lambda =$ 500 nm are $\varepsilon_{\mathrm{O}} = 2.776$ and $\varepsilon_{\mathrm{E}} = 2.219$ [40]. In Fig. 2(c) we show the time average of the optical chirality $\mathcal{C} = \frac{1}{2}[\mathbf{E}\cdot(\nabla\times\mathbf{D}) + \mathbf{H}\cdot(\nabla\times\mathbf{B})]$ as a function of the propagation coordinate z within a single anisotropic medium and of the impinging LP angle χ. This quantity is a measure of the local density of chirality of the EM field [41]. It was initially introduced as a first integral of Maxwell's equations in vacuum by Lipkin in 1964 [42], but was dismissed as holding no physical significance. However, the lines of a chiral field wrap around a central axis keeping a nontrivial component parallel to that axis, and thus later it has been understood that the optical chirality $\mathcal{C}$ embodies this geometrical picture [43,44]. The expression we use is the most complete form without any restrictions on the nature of the medium, as elaborated in Ref. [41]. Note that the optical chirality oscillates while the EM field propagates within the anisotropic medium, meaning that the polarization of the total EM field periodically changes helicity as a result of polarization beating produced by anisotropy. This is related to the fact that, fixing the extraordinary direction, there is no reason why the arbitrary polarization of the EM field should acquire one definite preferred helicity upon propagation. However, this can be engineered by adjusting the anisotropic medium thickness for fixed input polarization. Notice that for $\chi = 0, \pi/2$ the optical chirality vanishes, consistently with the considerations above pertaining Fig. 2(b). Figure 2(d) illustrates the z evolution

within the anisotropic medium of the forward and backward (FW and BW) waves polarization on the Poincaré sphere for $\chi = \pi/4$. This figure clearly shows that the EM polarization is not simply rotating, but it is actually periodically changing becoming elliptical, and eventually circular, which is exactly the underlying principle of $\lambda/4$ retarding wave plates. In Figs. 2(e) and 2(f) we illustrate the z dependence of time averaged (e) optical torque volume density and (f) effective torque per unit surface, defined as $\tau_{\rm S}^{(\rm EM)} = \int_0^z dz' \left\langle \boldsymbol{\tau}_{\rm V}^{\rm EM} \right\rangle_{\rm T} \cdot \hat{\mathbf{e}}_z$, for several distinct impinging LP angles χ. The behavior of these quantities is similar to the one of optical chirality in Fig. 2(c), that is, making exception for $\chi = 0, \pi/2$, they oscillate over z. This is due to the fact that, according to the sign of the cross product between the displacement vector and the electric field, i.e., according to the polarization of the field at a certain z, the optical torque can be either positive or negative and, due to the symmetry of the system, it does not have a preferred direction. Excitation by CP radiation of a single quarter-wave plate provides analogous results to LP reported in Fig. 2 owing to the CP beating produced by the wave plate. Indeed, as illustrated in Fig. 2(d), the polarization evolves periodically from circular to linear. In turn, CP excitation produces minor reflectance deviations and a phase shift of the oscillations observed in Fig. 2(d).

III. *N*-FOUR LAYERS

We here consider a TAPC composed of $N \times 4$ layers of $CaCO_3$. While our calculations below are suitable for a generic arrangement of extraordinary axes orientation in the x-y plane, we specialize them in a particular configuration where we progressively rotate by $\pi/4$ the extraordinary axis angle $\theta_{\rm E}^{(m)} = (m-1)\pi/4$, where the index $m = 1, 2, 3, 4$ indicates each layer within a four-layer stack, as depicted in Fig. 1. By solving Maxwell's equations in every layer, we can express the total electric field as

$$\mathbf{E}(\mathbf{r}, t) = \mathbf{E}_{\rm vac}(\mathbf{r}, t)\Theta(-z) + \mathbf{E}_{\rm vac}(\mathbf{r}_{\rm R}, t)\Theta[z - z_{\rm R}^{(N,4)}] + \sum_{n=1}^{N}\sum_{m=1}^{4}\left[\mathbf{E}_{\rm an}^{(+)}(\mathbf{r}_{\rm L}, t) + \mathbf{E}_{\rm an}^{(-)}(\mathbf{r}_{\rm L}, t)\right]\Theta_{\rm in}^{(n,m)}(z), \tag{8}$$

where $\mathbf{r}_{\rm L} = \mathbf{r} - z_{\rm L}^{(n,m)}\hat{\mathbf{e}}_z$, $\mathbf{r}_{\rm R} = \mathbf{r} - z_{\rm R}^{(N,4)}\hat{\mathbf{e}}_z$, $\Theta_{\rm in}^{(n,m)}(z) = \Theta(z - z_{\rm L}^{(n,m)}) - \Theta(z - z_{\rm R}^{(n,m)})$, and $z_{\rm L,R}^{(n,m)}$ indicate the left or right side positions of the mth layer within the nth four-layer stack. Analogous considerations hold for the magnetic field. We connect the field amplitudes using the transfer-matrix approach [37–39], as shown in Appendix A, and we evaluate numerically the full transfer matrix to calculate the reflectance and transmittance of the considered TAPC. By fixing the orientation of extraordinary axes shown in Fig. 1, we aim at transmitting as much RCP as possible of the impinging light, while reflecting the LCP one. To do so, we numerically optimize the thicknesses of layers at normal incidence with $N = 30$, obtaining $d_1 = 37.0$ nm, $d_2 = 54.2$ nm, $d_3 = 39.4$ nm, and $d_4 = 28.0$ nm. Our optimization procedure consists in the systematic quest for concurrent maxima of the left reflectance with impinging left circularly polarized radiation ($R_{\rm L}^{(\rm L)}$) and of the right transmittance with impinging right circularly polarized field ($T_{\rm R}^{(\rm R)}$). We iteratively vary the thicknesses of each layer in a range from 10 to 100 nm finding concurrent local maxima of the functional $R_{\rm L}^{(\rm L)} + T_{\rm R}^{(\rm R)}$, and then adjust the thickness ranges and steps to attain global maxima of $R_{\rm L}^{(\rm L)} + T_{\rm R}^{(\rm R)}$.

Before discussing multistack results, in Fig. 3 below we report numerical results obtained considering a single four-layer stack with $N = 1$ illuminated by RCP and LCP impinging light in order to illustrate the effect produced by a single building block of the total optical system on the optical chirality. Figure 3(a) shows the z dependence of the optical torque density, indicating an alternate

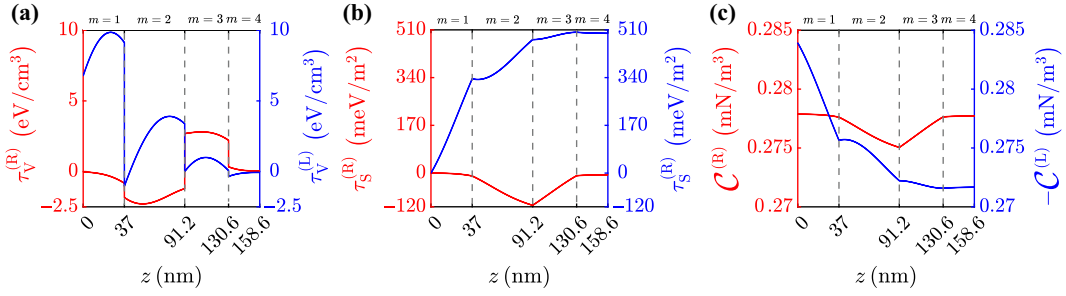

FIG. 3. EM field propagation within a single 4-layers stack of uniaxial anisotropic media. Each layer in every stack has a specific thickness d_m ($d_1 = 37.0$ nm, $d_2 = 54.2$ nm, $d_3 = 39.4$ nm, and $d_4 = 28.0$ nm) and a certain extraordinary angle $\theta_{\rm E}^{(m)} = (m-1)\pi/4$ with respect to the x-axis, which progressively rotates by $\pi/4$. The mirror is normally illuminated by an EM field with vacuum wavelength $\lambda = 500$ nm and either RCP/LCP (illustrated by red/blue curves, respectively). (a)–(c) Dependence of the (a) optical torque density, (b) effective optical torque per unit surface, and (c) the optical chirality over the propagation distance z.

dynamics averaging to vanishing net effect for RCP, which is confirmed by the z dependence of the effective optical torque per unit surface, see Fig. 3(b). Conversely, for LCP illumination, the optical torque density remains always positive while decreasing layer by layer. Given the general expression $\boldsymbol{\tau}_{\mathrm{V}}^{\mathrm{EM}} = -\mathbf{D} \times \mathbf{E}$, this phenomenon is related to the fact that the electric-field amplitudes of the two forward modes within the anisotropic medium are decreasing over propagation, i.e., light is undergoing Bragg reflection. Moreover, consistently with the optical torque density canceling out, in Fig. 3(b) the optical torque per unit surface is saturating to a giant positive value. To conclude, Fig. 3(c) shows that the optical chirality of RCP light at the end of the multilayer approximately amounts to the one at the beginning, while it increases for LCP light due to the torque action produced by the chiral system.

By increasing the number of multilayers one can amplify these effects reaching a near-unity reflectance for LCP and transmittance for RCP, thus engineering an integrated optical device capable of efficiently transmitting one CP while reflecting the other. In order to illustrate the potential functionalities of TAPCs, i.e., the capability to efficiently work concurrently as optical diodes for one CP and as helicity-preserving mirrors for the opposite CP, we maintain the orientation of the extraordinary axes illustrated in Fig. 1, but report the full results of the considered ($N = 30$) × 4-layer stack with the previously reported thicknesses (total thickness amounting to $d_{\mathrm{tot}} = 4.578$ μm, which should not impact the mechanical stability of the system) obtained through the systematic concurrent maximization of RCP transmittance and LCP reflectance. Numerical results are illustrated in Fig. 4. Note that, while RCP light is weakly affected by the anisotropy of the whole system, the LCP counterpart experiences a torque forcing the opposite handedness and leading to an almost complete reflection, see Figs. 4(a) and 4(b), as confirmed also by Fig. 4(c) illustrating the wavelength dependence of the averaged torque volume density upon RCP and LCP excitation. We emphasize that the addition of four-layer stacks amplifies the effect of the single-stack optical torque, see Figs. 3(a)–3(c) and 4(a)–4(c), owing to the efficient backscattering produced by the TAPC. Note that the stack thicknesses have been optimized at $\lambda = 500$ nm, providing maximized functionality, see Fig. 4(c) and Figs. 4(d) and 4(e) illustrating the reflectance and transmittance upon (d) LCP and (e) RCP illumination. We emphasize that the system can also be optimized to operate at distinct spectral regions and opposite impinging CP (e.g., setting a rotation of the anisotropic crystal axes over the opposite anticlockwise direction) by adjusting the stack thicknesses. From a fundamental perspective, such a process can be grasped by the z dependence of optical chirality, illustrated in Fig. 4(f), staying approximately constant for RCP illumination thanks to the preferential handedness imposed by the chiral mirror, while increasing towards zero upon LCP illumination. In turn, the TAPC forces LCP

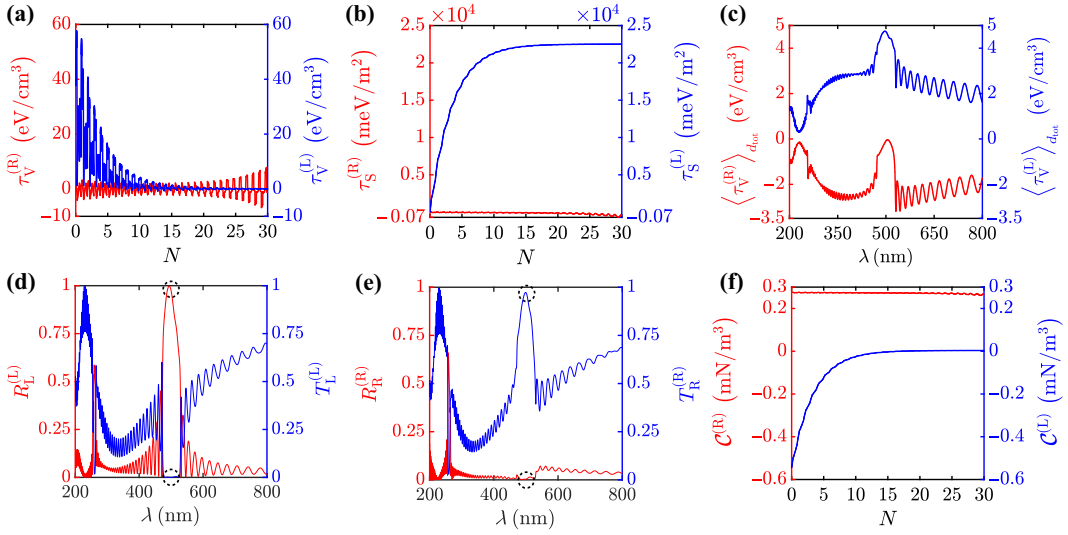

FIG. 4. EM field propagating within ($N = 30$) × 4-layer stack of uniaxial anisotropic media. (a) Dependence on the number of multilayers of the optical torque density for both normally incident RCP and LCP light. (b) Dependence on the number of multilayers of the optical torque per unit surface for both normally incident RCP and LCP light. (c) Wavelength dependence of the length average of the optical torque density for both normally incident RCP and LCP light. (d) Wavelength dependence of the reflectance and transmittance of LCP light with normally incident LCP light ($R_{\mathrm{L}}^{(\mathrm{L})}$ and $T_{\mathrm{L}}^{(\mathrm{L})}$, respectively). (e) Wavelength dependence of the reflectance and transmittance of RCP light with normally incident RCP light ($R_{\mathrm{R}}^{(\mathrm{R})}$ and $T_{\mathrm{R}}^{(\mathrm{R})}$, respectively). The dashed circles in (d),(e) indicate the reflectance and transmittance at $\lambda = 500$ nm. (f) Dependence on the number of multilayers of the optical chirality for both normally incident RCP and LCP light.

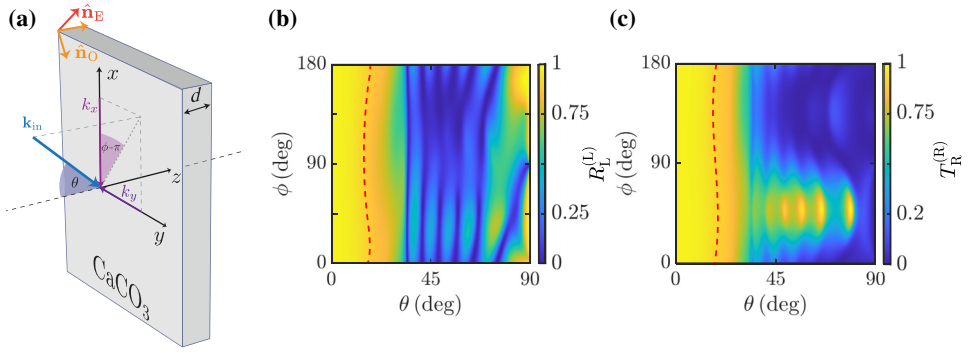

FIG. 5. Reflectance and transmittance for an EM field impinging with an arbitrary angle of incidence and propagating within $(N = 30) \times$ 4-layer stack of uniaxial anisotropic media. (a) Schematic illustration of the considered EM field azimuthal and zenithal angles of incidence. (b) Dependence of $R_L^{(L)}$ at $\lambda = 500$ nm over the angle of incidence. (c) Dependence of $T_R^{(R)}$ at $\lambda = 500$ nm over the angles of incidence. Note that for θ ranging from zero to the red dashed lines in (b),(c) $R_L^{(L)}, T_R^{(R)} > 0.90$.

impinging light to be completely reflected into LCP, as illustrated in Fig. 4(d) showing near-unity LCP reflectance $R_L^{(L)} = 0.998$ for $\lambda = 494.2$ nm. Note that, while such results are obtained at normal incidence, the considered TAPC possesses also a degree of omnidirectional features to some extent, as illustrated in Fig. 5(b) showing a LCP reflectance >90% within the cone $\theta \lesssim 20^\circ$. Moreover, Fig. 4(e) illustrates a very high RCP transmittance $T_R^{(R)} = 0.9728$ for $\lambda = 499$ nm. Again, such a chirally-sensitive functionality remains valid over a broad range of impinging zenithal angles $\theta \lesssim 20^\circ$ displaying RCP transmittance >90%, as illustrated in Fig. 5(c). Again, we emphasize that by adjusting the TAPC thicknesses, it is possible to attain optimal parameters providing maximum LCP reflectance and RCP transmittance (or vice versa, at will) at arbitrary angles of incidence.

However, as already mentioned, results illustrated in Figs. 4 and 5 are related to the configuration obtained after an appropriate optimization of the thicknesses of the slabs. In order to give a quantitative estimate of the uncertainty affecting reflectance and transmittance of the chiral mirror due to technologically achievable margins, we vary the configuration as follows. For each layer, we consider that the thickness could assume three possible values: the estimated one used in our previous simulations and the other two obtained with an error of ± 2 nm. Moreover, in order to account for errors in the orientation of extraordinary axes, we consider the values reported previously for $\theta_E^{(m)}$ and those obtained as $\pm 1^\circ$. In total, we have 3^8 configurations for a single TAPC building block. Averaging the reflectivities obtained over each of such configurations, we calculate the mean reflectance and transmittance with appropriate standard deviations, obtaining at $\lambda = 500$ nm $R_L^{(L)} = 0.92 \pm 0.08$ and $T_R^{(R)} = 0.91 \pm 0.06$, as illustrated in Fig. 6 aside. This indicates that TAPC functionalities are quite robust over crystal-orientation angles and thickness fluctuations. Regarding the practical realization of TAPCs, we emphasize that $CaCO_3$ crystals can be grown by mimicking nature and further adopted as optical functional materials [45], and some biological systems enable the growth to be perpendicular to the extraordinary axis [46]. In turn, the morphology of calcitic prisms is determined not only by the atomic structure of calcite, but largely by organic components, the presence or absence of which drastically affect the growth mode, thus suggesting

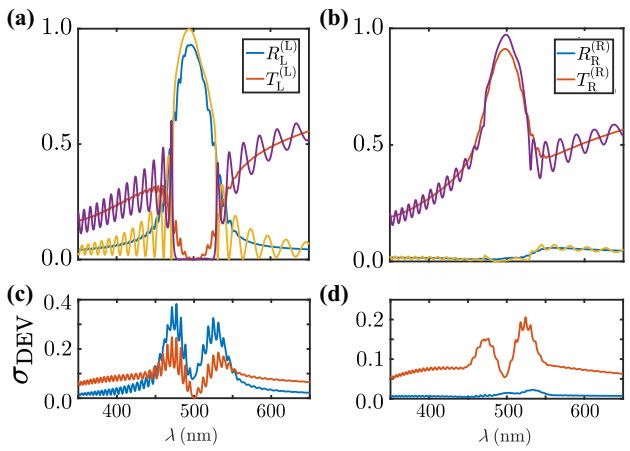

FIG. 6. Check for the robustness of the considered TAPC over crystal orientation angles and thicknesses fluctuations. (a) The smoother curves represent the averaged $R_L^{(L)}$ and $T_L^{(L)}$ over the unit stack configuration, while the others show the corresponding quantities with the optimized fixed parameters. Everything is plotted as a function of the excitation wavelength. (b) The smoother curves represent the averaged $R_R^{(R)}$ and $T_R^{(R)}$ over the unit stack configuration, while the others show the corresponding quantities with the optimized fixed parameters. Everything is plotted as a function of the excitation wavelength. (c) Wavelength dependence of the standard deviation associated with reflectance and transmittance of LCP light with normally incident LCP light. (d) Wavelength dependence of the standard deviation associated with the reflectance and transmittance of RCP light with normally incident RCP light.

the potential feasibility of calcite growth over a specific orientation. Thin films of calcite with a thickness of the order of tens of nanometers could be fabricated through a bottom-up approach consisting of an epitaxial growth process in which a thin film of calcite is formed on top of a sacrificial layer. For example, in Ref. [47] the growth of a thin calcium carbonate film was achieved by means of the atomic-layer chemical-vapor-deposition technique. This method has been demonstrated to provide a high degree of control over both the thickness of the film and the crystal orientation. We emphasize that to construct a stack in which each layer is rotated at a specific angle relative to the adjacent layers, it is essential to undertake efforts to identify which growth parameters can be altered to modify the crystal orientation along the growth axis. Another possible fabrication method could follow a top-down approach, namely the SmartCut^{TM} technology, which has been employed for the realization of thin layers of Si [48] and $LiNbO_3$ [49], which possesses the same space-group symmetry of calcite. The process is based on ion implantation (hydrogen, helium, argon, etc.) and wafer bonding, allowing for single-crystal layers to be transferred onto substrates. The diverse constituents of the four-layer stack could be aligned one over the other by means of a stacking machine, similarly to the fabrication of 2D material heterostructures. However, we emphasize that the choice of $CaCO_3$ in our calculations ensues from its large refractive-index step between ordinary and extraordinary waves, thus maximizing birefringence. We stress that our proposed TAPC concept does not rely on the particular anisotropic material choice and can straightforwardly rely on other materials. In general, however, to maximize miniaturization and preserve mechanical stability, highly birefringent materials such as $CaCO_3$ are desirable. Finally, in practical realizations one would be interested in zeroth-order and higher-order wave plates, but our theoretical calculations solely focus on the AM manipulation mechanism provided by TAPCs and does not focus on such potential advanced functionalities, which could be the subject of future investigations. Moreover, we stress that the concurrent maximization of one CP helicity-preserving reflectance and the opposite CP transmittance are practically attained by the engineering of phase shifts of the CP projections over ordinary and extraordinary axes for both forward and backward waves to produce CP-selective Bragg reflection. In turn, the proposed TAPCs are inherently narrowband, see Figs. 4(d) and 4(e), and this constitutes an inherent limitation of such systems. Nevertheless, the operational wavelength range can be tuned by the adjustment of the TAPC thicknesses.

IV. CONCLUSIONS

We have developed a general theoretical framework to describe propagation of monochromatic EM fields within TAPCs realized as twisted stacks of uniaxial anisotropic crystals. Our approach enables the evaluation of optical torques and polarization dynamics upon arbitrary impinging direction and orientation of the extraordinary axes of each layer. Furthermore, our theoretical framework enables high-performance CP-selective helicity-preserving mirrors to be devised based on TAPCs consisting of $CaCO_3$, an uniaxial anisotropic medium, with $\pi/4$-rotated extraordinary axes upon propagation. We find that, thanks to its extraordinarily efficient chirally sensitive Bragg resonances, such a system can operate as a CTU helicity-preserving mirror for one CP while concurrently enabling CTU transmittance of the opposite CP. This is accomplished by properly fixing the layer number and thicknesses. We further unveil that the effect of polarization splitting is a consequence of the optical torque density, which affects the EM field over its propagation within each anisotropic medium. Our results hold great promise for polarization control at the micro- and nanoscale. Owing to the operational functionalities of TAPCs, the potential applications range from the development of chirally selective cavities for chiroptical sensing to the management of CP of quantum emitters and many other applications involving CP manipulation.

ACKNOWLEDGMENTS

This work has been partially funded by the European Union—NextGenerationEU under the Italian Ministry of University and Research (MUR) National Innovation Ecosystem Grant No. ECS00000041—VITALITY—CUP E13C22001060006. This work has been supported by the European Union under Grant Agreement No. 101046424. Views and opinions expressed are however those of the author(s) only and do not necessarily reflect those of the European Union or the European Innovation Council. Neither the European Union nor the European Innovation Council can be held responsible for them.

DATA AVAILABILITY

The data that support the findings of this article are openly available [50]; embargo periods may apply.

APPENDIX: TRANSFER-MATRIX METHOD

As illustrated in the main text, we use the transfer-matrix approach to connect the field amplitudes at different interfaces. The refraction and reflection at the TAPC interfaces are accounted by three transfer matrices, i.e., from vacuum to an anisotropic medium layer (V-AN), between two distinct layers (AN-AN), and from the last layer to vacuum (AN-V). Adopting the index $m = 1, 2, 3, 4$ to label each layer in a single four-layer stack, we insert the appropriate expressions for the EM field in the boundary conditions constraints, i.e., Eq. (1) for the vacuum field and Eqs. (4)

and (5) for the modes within the anisotropic medium to obtain the V-AN ($m = 1$) and the AN-V transfer matrices ($m = 4$), while Eqs. (4) and (5) specialize to two different anisotropic layers for the AN-AN matrix ($m = i,j$, with $i \neq j$). Thus, the boundary conditions for the continuity of (i) magnetic field, (ii) normal component of the displacement vector, and (iii) tangential components of the electric field, provide what is reported in Eq. (A1), where in the second equality $j, i = 1,2,3,4$, with $j \neq i$, and in the last one T denotes the transmitted wave amplitudes.

$$\hat{M}_{\rm vac}\begin{bmatrix} A_1^{(\rm I)} \\ A_{-1}^{(\rm I)} \\ A_1^{(\rm R)} \\ A_{-1}^{(\rm R)} \end{bmatrix} = \hat{M}_1 \begin{bmatrix} A_1^{(+,1)} \\ A_2^{(+,1)} \\ A_1^{(-,1)} \\ A_2^{(-,1)} \end{bmatrix},$$
$$\hat{M}_i \begin{bmatrix} A_1^{(+,i)} \\ A_2^{(+,i)} \\ A_1^{(-,i)} \\ A_2^{(-,i)} \end{bmatrix} = \hat{M}_j \begin{bmatrix} A_1^{(+,j)} \\ A_2^{(+,j)} \\ A_1^{(-,j)} \\ A_2^{(-,j)} \end{bmatrix}, \qquad \text{(A1)}$$

$$\hat{M}_4 \begin{bmatrix} A_1^{(+,4)} \\ A_2^{(+,4)} \\ A_1^{(-,4)} \\ A_2^{(-,4)} \end{bmatrix} = \hat{M}_{\rm vac} \begin{bmatrix} A_1^{(\rm T)} \\ A_{-1}^{(\rm T)} \\ 0 \\ 0 \end{bmatrix}.$$

In particular,

$$\hat{M}_{\rm vac} = \mathcal{N} \begin{bmatrix} 1 & 1 & 1 & 1 \\ M_{\rm vac}^{(-)} & -M_{\rm vac}^{(+)} & -M_{\rm vac}^{(+)} & M_{\rm vac}^{(-)} \\ -ik_{\rm I} & ik_{\rm I} & -ik_{\rm I} & ik_{\rm I} \\ -ik_{\rm I}M_{\rm vac}^{(-)} & -ik_{\rm I}M_{\rm vac}^{(+)} & ik_{\rm I}M_{\rm vac}^{(+)} & ik_{\rm I}M_{\rm vac}^{(-)} \end{bmatrix}, \qquad \text{(A2)}$$

where $M_{\rm vac}^{(\pm)} = (ik_{\rm I}k_{\rm Iz} \pm k_{\rm Ix}k_{\rm Iy})/(k_{\rm Iz}^2 + k_{\rm Iy}^2)$, $\mathcal{N} = \sqrt{(k_{\rm Iz}^2 + k_{\rm Iy}^2)/\left(2k_{\rm I}^2\right)}$ and

$$\hat{M}_m = \begin{bmatrix} \frac{\sin\theta_{\rm E}^{(m)}\beta_1^{(m)}}{D_1^{(m)}} & \frac{\frac{\omega^2}{c^2}\cos\theta_{\rm E}^{(m)} - \frac{k_{\rm Ix}}{\varepsilon_{\rm O}^{(m)}}\alpha^{(m)}}{D_2^{(m)}} & \frac{\sin\theta_{\rm E}^{(m)}\beta_1^{(m)}}{D_1^{(m)}} & \frac{\frac{\omega^2}{c^2}\cos\theta_{\rm E}^{(m)} - \frac{k_{\rm Ix}}{\varepsilon_{\rm O}^{(m)}}\alpha^{(m)}}{D_2^{(m)}} \\ -\frac{\cos\theta_{\rm E}^{(m)}\beta_1^{(m)}}{D_1^{(m)}} & \frac{\frac{\omega^2}{c^2}\sin\theta_{\rm E}^{(m)} - \frac{k_{\rm Iy}}{\varepsilon_{\rm O}^{(m)}}\alpha^{(m)}}{D_2^{(m)}} & -\frac{\cos\theta_{\rm E}^{(m)}\beta_1^{(m)}}{D_1^{(m)}} & \frac{\frac{\omega^2}{c^2}\sin\theta_{\rm E}^{(m)} - \frac{k_{\rm Iy}}{\varepsilon_{\rm O}^{(m)}}\alpha^{(m)}}{D_2^{(m)}} \\ \frac{\frac{\omega^2}{c^2}\varepsilon_{\rm O}^{(m)}\cos\theta_{\rm E}^{(m)} - k_{\rm Ix}\alpha^{(m)}}{D_1^{(m)}} & -\frac{\frac{\omega^2}{c^2}\sin\theta_{\rm E}^{(m)}\beta_2^{(m)}}{D_2^{(m)}} & -\frac{\frac{\omega^2}{c^2}\varepsilon_{\rm O}^{(m)}\cos\theta_{\rm E}^{(m)} - k_{\rm Ix}\alpha^{(m)}}{D_1^{(m)}} & \frac{\frac{\omega^2}{c^2}\sin\theta_{\rm E}^{(m)}\beta_2^{(m)}}{D_2^{(m)}} \\ \frac{\frac{\omega^2}{c^2}\varepsilon_{\rm O}^{(m)}\sin\theta_{\rm E}^{(m)} - k_{\rm Iy}\alpha^{(m)}}{D_1^{(m)}} & \frac{\frac{\omega^2}{c^2}\cos\theta_{\rm E}^{(m)}\beta_2^{(m)}}{D_2^{(m)}} & -\frac{\frac{\omega^2}{c^2}\varepsilon_{\rm O}^{(m)}\sin\theta_{\rm E}^{(m)} - k_{\rm Iy}\alpha^{(m)}}{D_1^{(m)}} & -\frac{\frac{\omega^2}{c^2}\cos\theta_{\rm E}^{(m)}\beta_2^{(m)}}{D_2^{(m)}} \end{bmatrix}. \qquad \text{(A3)}$$

In the chosen anisotropic crystal mode basis, in-layer propagation matrices are easily obtained as $\hat{P}_m = \text{diag}\left[e^{i\beta_1^{(m)}d_m}, e^{i\beta_2^{(m)}d_m}, e^{-i\beta_1^{(m)}d_m}, e^{-i\beta_2^{(m)}d_m}\right]$. This allows us to solve the linear problem for the amplitudes and express the field on one side of the mirror in terms of the field on the other side, that is

$$\begin{bmatrix} A_1^{(\rm T)} \\ A_{-1}^{(\rm T)} \\ 0 \\ 0 \end{bmatrix} = \hat{M}_{4\to\rm vac}\hat{P}_4\hat{M}_{3\to4}\hat{P}_3\hat{M}_{2\to3}\hat{P}_2\hat{M}_{1\to2}\hat{P}_1 \left(\hat{M}_{4\to1}\hat{P}_4\hat{M}_{3\to4}\hat{P}_3\hat{M}_{2\to3}\hat{P}_2\hat{M}_{1\to2}\hat{P}_1\right)^{N-1}\hat{M}_{\rm vac\to1}\begin{bmatrix} A_1^{(\rm I)} \\ A_{-1}^{(\rm I)} \\ A_1^{(\rm R)} \\ A_{-1}^{(\rm R)} \end{bmatrix}, \qquad \text{(A4)}$$

where $\hat{M}_{\rm vac\to1} = \left(\hat{M}_1\right)^{-1}\hat{M}_{\rm vac}$, $\hat{M}_{i\to j} = \left(\hat{M}_j\right)^{-1}\hat{M}_i$, and $\hat{M}_{4\to\rm vac} = \left(\hat{M}_{\rm vac}\right)^{-1}\hat{M}_4$. Eventually, we obtain the reflectance and transmittance for RCP and LCP as $R^{(\rm R,L)} = \left|A_{\pm1}^{(\rm R)}\right|^2 \Big/ \left(\left|A_1^{(\rm I)}\right|^2 + \left|A_{-1}^{(\rm I)}\right|^2\right)$, $T^{(\rm R,L)} = \left|A_{\pm1}^{(\rm T)}\right|^2 \Big/ \left(\left|A_1^{(\rm I)}\right|^2 + \left|A_{-1}^{(\rm I)}\right|^2\right)$. In turn, results reported in Figs. 2–6 of the main text are obtained by the numerical inversion of the scattering matrix $\hat{S}$ [37–39], connecting reflected and transmitted CP EM wave components to impinging CP ones, by rearranging the entries of the total transfer matrix in Eq. (A4).

[1] R. W. Woody, Circular dichroism, Methods Enzymol. **246**, 34 (1995).

[2] N. Berova, K. Nakanishi, and R. W. Woody, *Circular Dichroism: Principles and Applications* (John Wiley & Sons, New York, 2000).

[3] H. Eyring, H. C. Liu, and D. Caldwell, Optical rotatory dispersion and circular dichroism, Chem. Rev. **68**, 525 (1968).

[4] M. Schäferling, Chirality in Nature and Science, Springer Ser. Opt. Sci. **205**, 5 (2017).

[5] Y. Luo, C. Chi, M. Jiang, R. Li, S. Zu, Y. Li, and Z. Fang, Plasmonic chiral nanostructures: Chiroptical effects and applications, Adv. Opt. Mater. **5**, 1700040 (2017).

[6] M. Qiu, L. Zhang, Z. Tang, W. Jin, C. W. Qiu, and D. Y. Lei, 3D metaphotonic nanostructures with intrinsic chirality, Adv. Funct. Mater. **28**, 1803147 (2018).

[7] H. S. Khaliq, A. Nauman, J. W. Lee, and H. R. Kim, Recent progress on plasmonic and dielectric chiral metasurfaces: Fundamentals design strategies, and implementation, Adv. Opt. Mater. **11**, 2300644 (2023).

[8] D. Sievenpiper, L. Zhang, R. F. J. Broas, N. G. Alexopolous, and E. Yablonovitch, High-impedance electromagnetic surfaces with a forbidden frequency band, IEEE Trans. Antennas Propag. **47**, 2059 (1999).

[9] A. P. Feresidis, G. Goussetis, S. Wang, and J. C. Vardaxoglou, Artificial magnetic conductor surfaces and their application to low-profile high-gain planar antennas, IEEE Trans. Antennas Propag. **53**, 209 (2005).

[10] D. J. Kern, D. H. Werner, A. Monorchio, L. Lanuzza, and M. J. Wilhelm, The design synthesis of multiband artificial magnetic conductors using high impedance frequency selective surfaces, IEEE Trans. Antennas Propag. **53**, 8 (2005).

[11] V. A. Fedotov, A. V. Rogacheva, N. I. Zheludev, P. L. Mladyonov, and S. L. Prosvirnin, Mirror that does not change the phase of reflected waves, Appl. Phys. Lett. **88**, 091119 (2006).

[12] S. Xiao, H. Mühlenbernd, G. Li, M. Kenney, F. Liu, T. Zentgraf, S. Zhang, and J. Li, Helicity-preserving omnidirectional plasmonic mirror, Adv. Opt. Mater. **4**, 654 (2016).

[13] X. Zheng, Z. Xiao, and X. Ling, A tunable hybrid metamaterial reflective polarization converter based on vanadium oxide film, Plasmonics **13**, 287 (2018).

[14] J. K. Gansel, M. Thiel, M. S. Rill, M. Decker, K. Bade, V. Saile, G. V. Freymann, S. Linden, and M. Wegener, Gold helix photonic metamaterial as broadband circular polarizer, Science **325**, 1513 (2009).

[15] Y. Zhao, M. A. Belkin, and A. Alù, Twisted optical metamaterials for planarized ultrathin broadband circular polarizers, Nat. Commun. **3**, 870 (2012).

[16] I. Lindell, A. Sihvola, S. Tretyakov, and A. J. Viitanen, *Electromagnetic Waves in Chiral and Bi-Isotropic Media* (Artech House, Boston, 1994).

[17] L. Tsang, J. A. Kong, and K. H. Ding, *Scattering of Electromagnetic Waves: Theories and Applications* (Wiley, New York, 2000).

[18] J. Dong, J. Zhou, T. Koschny, and C. Soukoulis, Bilayer cross chiral structure with strong optical activity and negative refractive index, Opt. Express **17**, 14172 (2009).

[19] Y. Zhao, A. N. Askarpour, L. Sun, J. Shi, X. Li, and A. Alù, Chirality detection of enantiomers using twisted optical metamaterials, Nat. Commun. **8**, 14180 (2017).

[20] Z. Han, F. Wang, J. Sun, X. Wang, and Z. Tang, Recent advances in ultrathin chiral metasurfaces by twisted stacking, Adv. Mater. **35**, 2206141 (2023).

[21] M. T. Enders, M. Sarkar, E. Klironomou, M. F. Picardi, A. Deeva, and G. T. Papadakis, Intrinsic mid-IR chirality and chiral thermal emission from twisted bilayers, ArXiv:2409.02641.

[22] M. Hentschel, M. Schäferling, X. Duan, H. Giessen, and N. Liu, Chiral plasmonics, Sci. Adv. **3**, e1602735 (2017).

[23] X. T. Kong, L. V. Besteiro, Z. Wang, and A. O. Govorov, Plasmonic chirality and circular dichroism in bioassembled and nonbiological systems: Theoretical background and recent progress, Adv. Mater. **32**, 1801790 (2020).

[24] Y. Fink, J. N. Winn, S. Fan, C. Chen, J. Michel, J. D. Joannopoulos, and E. L. Thomas, A dielectric omnidirectional reflector, Science **282**, 1679 (1998).

[25] S. Jahani and Z. Jacob, All-dielectric metamaterials, Nat. Nanotechnol. **11**, 23 (2016).

[26] S. Kruk and Y. Kivshar, Functional meta-optics and nanophotonics governed by Mie resonances, ACS Photonics **4**, 2638 (2017).

[27] Y. Kivshar, All-dielectric meta-optics and non-linear nanophotonics, Natl. Sci. Rev. **5**, 144 (2018).

[28] Z. Li, W. Liu, H. Cheng, D. Y. Choi, S. Chen, and J. Tian, Spin-selective full-dimensional manipulation of optical waves with chiral mirror, Adv. Mater. **32**, 1907983 (2019).

[29] X. Ma, M. Pu, X. Li, C. Huang, Y. Wang, W. Pan, B. Zhao, J. Cui, C. Wang, Z. Zhao, and X. Luo, A planar chiral metasurface for optical vortex generation and focusing, Sci. Rep. **5**, 10365 (2015).

[30] H. Ahmed, H. Kim, Y. Zhang, Y. Intaravanne, J. Jang, J. Rho, S. Chen, and X. Chen, Optical metasurfaces for generating and manipulating optical vortex beams, Nanophotonics **11**, 941 (2022).

[31] I. J. Hodgkinson, M. Arnold, M. W. McCall, and A. Lakhtakia, Chiral mirror and optical resonator designs for circularly polarized light: Suppression of cross-polarized reflectances and transmittances, Opt. Commun. **210**, 201 (2002).

[32] M. Pu, P. Chen, Y. Wang, Z. Zhao, C. Huang, C. Wang, X. Ma, and X. Luo, Anisotropic meta-mirror for achromatic electromagnetic polarization manipulation, Appl. Phys. Lett. **102**, 131906 (2013).

[33] E. Plum and N. I. Zheludev, Chiral mirrors, Appl. Phys. Lett. **106**, 221901 (2015).

[34] J. Hwang, M. H. Song, B. Park, S. Nishimura, T. Toyooka, J. W. Wu, Y. Takanishi, K. Ishikawa, and H. Takezoe, Electro-tunable optical diode based on photonic bandgap liquid-crystal heterojunctions, Nat. Mater. **4**, 383 (2005).

[35] M. Thiel, M. Decker, M. Deubel, M. Wegener, S. Linden, and G. von Freymann, Polarization stop bands in chiral polymeric three-dimensional photonic crystals, Adv. Mater. **19**, 207 (2007).

[36] R. A. Beth, Mechanical detection and measurement of the angular momentum of light, Phys. Rev. **50**, 115 (1936).

[37] P. Yeh, Electromagnetic propagation in birefringent layered media, JOSA **69**, 742 (1979).
[38] P. Yeh, Optics of anisotropic layered media: A new 4×4 matrix algebra, Surf. Sci. **96**, 41 (1980).
[39] P. Yeh and J. Tracy, Theory of dispersive birefringent filters, Imaging Spectrosc. I **268**, 171 (1981).
[40] G. Ghosh, Dispersion-equation coefficients for the refractive index and birefringence of calcite and quartz crystals, Opt. Commun. **163**, 95 (1999).
[41] J. E. Vázquez-Lozano and A. Martínez, Optical chirality in dispersive and lossy media, Phys. Rev. Lett. **121**, 043901 (2018).
[42] D. M. Lipkin, Existence of a new conservation law in electromagnetic theory, J. Math. Phys. (New York, US) **5**, 696 (1964).
[43] Y. Tang and A. E. Cohen, Optical chirality and its interaction with matter, Phys. Rev. Lett. **104**, 163901 (2010).
[44] Y. Tang and A. E. Cohen, Enhanced enantioselectivity in excitation of chiral molecules by superchiral light, Science **332**, 333 (2011).
[45] I. Schmidt and W. Wagermaier, Tailoring calcium carbonate to serve as optical functional material: Examples from biology and materials science, Adv. Mater. Interfaces **4**, 1600250 (2017).
[46] Y. Dauphin, E. Zolotoyabko, A. Berner, E. Lakin, C. Rollion-Bard, J. P. Cuif, and P. Fratzl, Breaking the long-standing morphological paradigm: Individual prisms in the pearl oyster shell grow perpendicular to the *c*-axis of calcite, J. Struct. Biol. **205**, 121 (2019).
[47] O. Nilsen, H. Fjellvåg, and A. Kjekshus, Growth of calcium carbonate by the atomic layer chemical vapour deposition technique, Thin Solid Films **450**, 240 (2004).
[48] H. Moriceau, F. Mazen, C. Braley, F. Rieutord, A. Tauzin, and C. Deguet, Smart Cut^{TM}: Review on an attractive process for innovative substrate elaboration, Nucl. Instrum. Methods Phys. Res. B **277**, 84 (2012).
[49] Z. Fang, H. Jin, S. Dong, L. Lu, W. Xuan, and J. Luo, Ultrathin single-crystalline $LiNbO_3$ film bulk acoustic resonator for 5G communication, Electron. Lett. **56**, 1142 (2020).
[50] A. Alessandrini, L. di Mauro Villari, L. Assogna, M. Silvestri, M. Venturi, C. Ferrante, P. Benassi, D. Tedeschi, and A. Marini, Zenodo (2025), https://doi.org/10.5281/zenodo.15366612.